Soot formation and temperature structure in small methane–oxygen diffusion flames at subcritical and supercritical pressures

Hyun I. Joo, Ömer L. Gülder *

University of Toronto, Institute for Aerospace Studies, 4925 Dufferin Street, Toronto, Ont., Canada M3H 5T6

A B S T R A C T

An experimental study was conducted to examine the characteristics of laminar methane–oxygen diffusion flames up to 100 atmospheres. The influence of pressure on soot formation and on the structure of the temperature field was investigated over the pressure range of 10–90 atmospheres in a high-pressure combustion chamber using a non-intrusive, line-of-sight spectral soot emission diagnostic technique. Two distinct zones characterized the appearance of a methane and pure oxygen diffusion flame: an inner luminous zone similar to the methane–air diffusion flames, and an outer diffusion flame zone which is mostly blue. The flame height, marked by the visible soot radiation emission, was reduced by over 50% over the pressure range of 10–100 atmospheres. Between 10 and 40 atmospheres, the soot levels increased with increasing pressure; however, above 40 atmospheres the soot concentrations decreased with increasing pressure.

1. Introduction

Our understanding of high-pressure combustion is relatively limited in spite of the fact that most practical combustion and propulsion devices operate at high pressures. One of the major causes of this is the non-trivial nature of tractable high-pressure combustion experiments [1,2] and simulations [3]. Experimental data on high-pressure laminar diffusion flames of gaseous fuels in air have become available only very recently at pressures above 10 atmospheres (atm) [4–7]. In most practical diffusion combustion systems, the combustion is turbulent. However, the high level of intermittency due to turbulent motion and relatively short residence times involved in these flames are not always suitable for experimental measurements of combustion events like soot formation. One of the widely used approximate approaches is to make use of the similarities in laminar and turbulent diffusion flames. One very popular approach is the laminar flamelet concept that provides a tractable flame model. As a result, most of the soot measurements are made in laminar diffusion flames that provide easily controlled conditions and the results can be projected to practical turbulent flames.

Effects of pressure on combustion in general and on pollutant formation in particular are significant and cannot be neglected. Combustion of fuels in pure oxygen is not widely used except in very niche aerospace applications such as liquid propellant rocket engines. A recent interest is the potential use of methane and li-

quid oxygen as propellants for reusable rocket engines [8]. The rationale is to reduce operational costs as well as overall propellant tank sizes as compared to liquid hydrogen. For the development of future launch vehicles hydrocarbon propellants are being considered especially for applications in booster or core stage engines. Liquid oxygen–methane is viewed as one of the most promising propellant combinations in this context [8].

To our knowledge, there is not much information on the structure and characteristics of co-flow laminar diffusion flames of methane in oxygen at pressures above atmospheric in open literature. Most of the research done at atmospheric pressure is related to oxy-fuel combustion applications and the interest is in the use of oxygen enriched air as the oxidizer. The effect of oxygen concentration in the co-flow air on soot formation in laminar diffusion flames of methane at atmospheric conditions was reported by Sugiyama [9] and Lee et al. [10]. It is argued in [9] that the observed reductions in soot concentrations upon increasing the oxygen concentration in co-flow air is due to the changes in velocity field and in the flame shape. In [10] it is reported that the soot surface growth and oxidation rates are higher in flames of methane with an oxidizer consisting of 50% oxygen–50% nitrogen compared to the rates in a methane–air base flame. Soot concentrations are reduced as the oxygen concentration in the oxidizer is increased [10]. Du et al. [11] reported that in a counter-flow diffusion flame the effect of oxygen concentration on the oxidizer side, for both ethylene and propane flames, is almost totally thermal. A recent numerical study [12] considers a counter-flow geometry flame of liquid oxygen and methane at transcritical conditions. Flame structures, namely major and minor species concentrations, are calculated at

* Corresponding author. Fax: +1 416 667 7799.
  E-mail address: ogulder@utias.utoronto.ca (Ö.L. Gülder).

7 MPa (about 70 atm) for three scenarios of liquid oxygen and methane injection temperatures.

Studies conducted on turbulent conditions at supercritical methane pressures with liquid oxygen are all related to rocket applications [12–14]. Liquefied methane has some favorable cooling characteristics that can be used in combustion chambers with regenerative cooling [13]. However, if the cooling jacket temperature exceeds 1000 K methane tends to decompose fast and form carbon deposits [14].

The objective of this study is to investigate the structure of the methane–oxygen co-flow diffusion flames from subcritical to supercritical pressures, up to 100 atm. The physical flame appearance as well as the sooting characteristics and temperature field of the flames as affected by pressure are presented and discussed. This study complements the research work reported in [4–7] and extends our understanding of high-pressure soot formation from gaseous hydrocarbon–air diffusion flames to flames of methane in pure oxygen.

2. Experimental methodology

Experiments were conducted in a high-pressure combustion chamber with an inner diameter of 0.24 m and a height of 0.60 m [5,7]. The combustion chamber has a design pressure of 110 atm and its schematic is shown in Fig. 1. Optical access to the chamber is provided through three quartz glass view-ports of equal diameter located at 0°, 90° and 180° that allows line-of-sight and 90° scattering and imaging measurements. The co-flow burner shown in Fig. 2 is comprised of a stainless steel fuel nozzle with an exit tip diameter of 3.06 mm and an air nozzle diameter of 25 mm. Sintered metal foam is included in the fuel and air nozzles to reduce the flow instabilities and to achieve a top-hat exit velocity profile as the gases leave the foam elements. To ensure careful con-
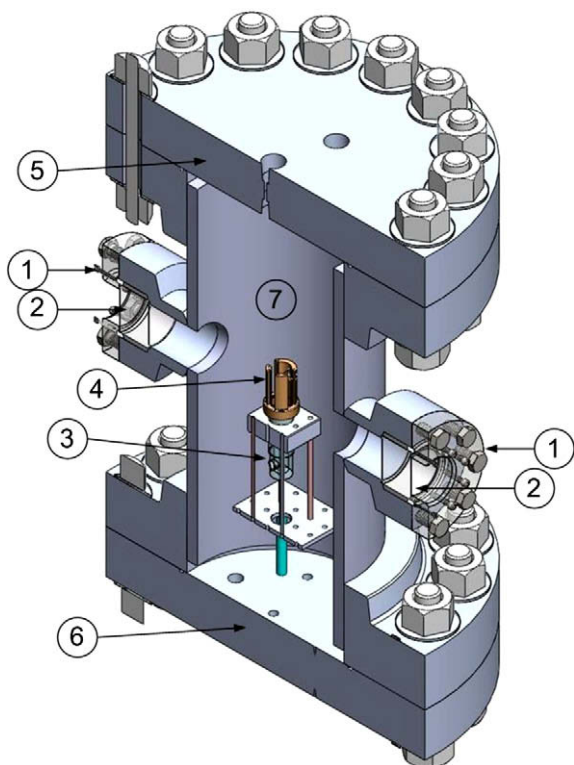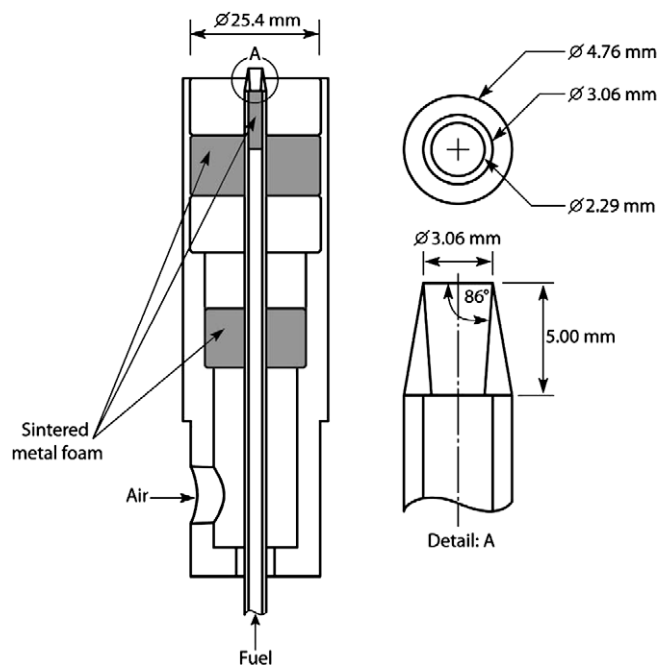

Fig. 2. Details of the co-flow burner.

trol of the fuel nozzle surface, the burner was routinely examined and cleaned after use. Prior to starting any experiment the contents of the combustion chamber were purged with pure oxygen to remove any residual gases from the previous experiment. A chimney was used to extend the length of the air co-flow nozzle and to shield the flame from ambient fluid perturbations. The flame is ignited using a glow plug inserted into the chimney that is located about 28 mm above the fuel nozzle. Once the flame is established at atmospheric pressure, the combustion chamber is pressurized by introducing pure oxygen directly into the chamber space. Measurements were collected as soon as the system reached the set pressure. Methane (99% purity) and oxygen gas (99.6% purity) were used for all the experiments. A thermal-based mass flow controller was used to deliver constant rate of methane to the burner. Constant methane mass flow rate of 1.1 mg/s (unless specified otherwise) that correspond to carbon mass flow rate of 0.824 mg/s was used. The thermal-based mass flow meter is calibrated for high pressure use and has a maximum total error of less than 2% up to 50 atm and about 6% between 50 and 100 atm.

Still and motion pictures were captured using a single-lens reflex camera with a standard macro-lens and a video camera for all the pressures from 1 to 100 atm. The main purpose of the video recordings was to check the flame stability during the measurements. For all the images, aperture and exposure time were adjusted to prevent image-saturation and thus a relatively constant intensity was maintained for all the images.

A non-intrusive, line-of-sight spectral soot emission (SSE) diagnostic technique was used to obtain the temperature and the soot volume fraction. In SSE diagnostic, line-of-sight radiation emissions from soot are measured along chords through the flame at a given height. The lateral emission scans are inverted to obtain radially resolved emission data using the three-point Abel deconvolution technique, where temperature and soot volume fraction can be determined when soot optical properties are known [15]. Soot radiation emissions are measured every 50 μm across the flame at the height increments of 0.5 mm. Details of the theory are provided elsewhere [16] and the specifics of the overall experimental layout of the spectral soot emission diagnostic used in this study are provided by Joo and Gülder [7].

Fig. 1. A cutaway view of the high-pressure chamber: (1) optical access ports; (2) quartz windows; (3) burner assembly; (4) chimney assembly; (5) upper flange housing the exhaust, safety valves, and pressure transducer; (6) Lower flange housing air, fuel pipes and wiring and (7) combustion chamber.

3. Results and discussion

3.1. Flame appearance

Two distinct zones characterized the appearance of a methane–oxygen diffusion flame: an inner luminous zone of yellow–orange color which is typical of laminar diffusion flames of hydrocarbons in air, and an outer mostly blue flame zone, Fig. 3. At atmospheric pressure the luminous zone appeared as a semi-sphere and attached to the burner rim by the typical blue region, similar to that of an atmospheric hydrocarbon–air diffusion flame. The yellow sooting region was concentrated mainly towards the tip of the luminous zone and the entire zone was encapsulated by a much larger blue flame with a bulbous appearance. In diffusive combustion of methane in oxygen, methane's oxidative pyrolysis is expected to lead to formation of hydrogen which can quickly diffuse through the reaction zone [17] and form the non-sooting flame enclosing the luminous zone, Fig. 3. At atmospheric methane–air diffusion flames, a very thin layer of a blue flame enclosing the yellow luminous diffusion flame was reported by Saito et al. [18] at low methane flow rates.

To assess the nature of the blue flame zone an axysymmetric flame code [19,20] was used to calculate the species concentrations and flame temperatures of methane–air and methane–oxygen diffusion flames at atmospheric pressure. Soot formation and radiation were turned off and the chemical kinetics were handled by using GRI-Mech 3.0. Further details of the code are given in [19,20]. Centerline temperature profiles along the flame axis for both flames are shown in Fig. 4. As expected, the maximum centerline temperature of methane–oxygen flame is about 700–800 K higher than that of methane–air flame. Centerline hydrogen mass fractions along the flame axis indicate that relatively large amounts of hydrogen are produced through the pyrolysis of methane at high temperatures in methane–oxygen flame as compared to the methane–air flame, Fig. 4. Heights of the two zones measured along the flame axis, Fig. 3b, are superimposed on the hydrogen mass fraction profile of methane–oxygen flame in Fig. 4. It seems that the mass fraction of hydrogen reaches a peak at the tip of the yellow luminous zone and then hydrogen is depleted by oxygen through a dif-
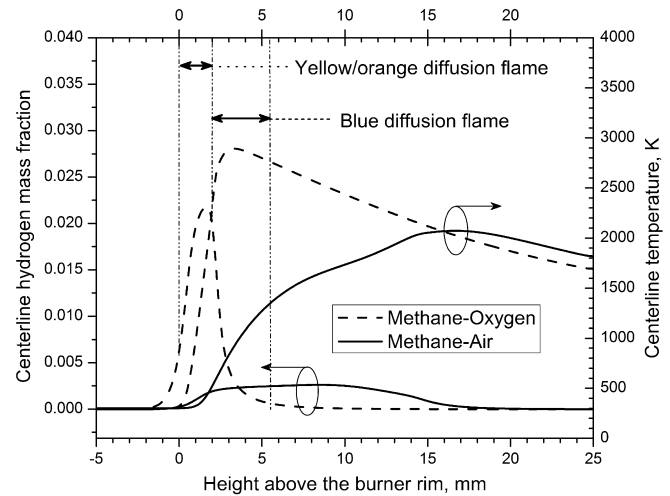

Fig. 4. Temperature and hydrogen mass fraction profiles along the flame centerlines in methane–air and methane–oxygen flames computed by an axysymmetric diffusion flame code at atmospheric pressure. Methane flow rate is 1.1 mg/s. Horizontal arrows indicate the measured heights of the yellow/orange and blue zones in methane–oxygen flames as shown in Fig. 3.

fusion flame within the blue flame zone. A similar behavior was observed with the mass fraction of carbon monoxide as shown in Fig. 5. Carbon monoxide concentration reached a peak, similar to hydrogen, at the tip of yellow luminous zone. Then it was oxidized, along with hydrogen, by oxygen diffusing inwards within the blue flame zone. Only a small fraction seemed to exit the blue flame tip, Fig. 5. These observations confirm that the blue flame zone is mainly a diffusion flame of hydrogen and carbon monoxide burning in oxygen. However, the computed oxygen mass fraction along the flame centerline increased from basically zero at the tip of the yellow zone and the beginning of the blue zone, Fig. 5, to high concentrations before the tip of the blue zone. This indicates that the blue zone is a diffusion flame as it starts above the yellow zone but turns into a partially premixed (stratified) flame with height as a result of intense diffusion of oxygen into the flame zone.
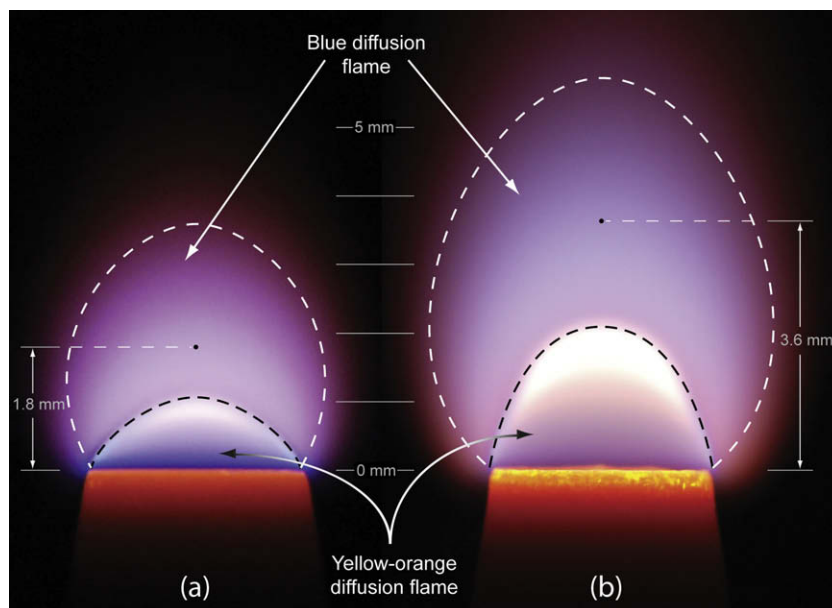

Fig. 3. Pictures of the methane–oxygen flames with highlighted boundaries of two zones: (a) methane flow rate 0.55 mg/s and (b) methane flow rate 1.1 mg/s. Heights denoted by 1.8 mm and 3.6 mm correspond to heights calculated by using Roper's equation [21]. (For interpretation of the references to color in this figure legend, the reader is referred to the web version of this article.)
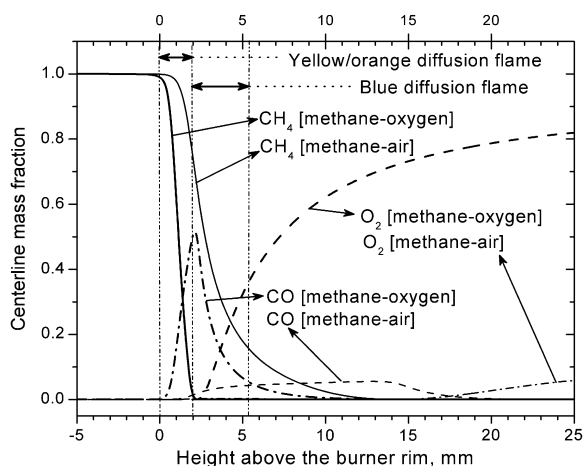
Fig. 5. Methane, carbon monoxide, and oxygen mass fraction profiles along the flame centerlines in methane–air and methane–oxygen flames computed by an axysymmetric diffusion flame code at atmospheric pressure. Methane flow rate is 1.1 mg/s. Horizontal arrows indicate the measured heights of the yellow/orange and blue zones in methane–oxygen flames as shown in Fig. 3.

With increasing pressure the sooting region expanded towards the fuel nozzle and the luminous zone appeared to be attached to the fuel nozzle, Fig. 6. The flame became conical in shape at higher pressures and the cross-sectional area of the flame decreased to give a pinched appearance to the flame. The height of the luminous zone, however, decreased steadily as the pressure was increased to 50 atm, Fig. 6. At 60 atm and above, the height remained relatively constant at about 1 mm. Overall, increasing the pressure from 10 to 100 atm resulted in over 50% reduction in the height of the luminous zone. This was an unexpected result in view of the previous measurements with methane–air diffusion flames. In methane–air diffusion flames, the luminous flame height is observed to stay almost constant from 10 to 100 atm [7].

It is shown that, to a first approximation, the height of a buoyancy-dominated laminar co-flow diffusion flame, established on a circular fuel nozzle, scales with molecular diffusivity, D, fuel flow rate, Q, mean flame temperature, T_f, and molar stoichiometric oxidizer to fuel ratio, S, as [21],

$$H \propto \frac{Q/T_f^{0.67}}{D\ln(1+1/S)} \propto \frac{1}{PT_f^{0.67}} \frac{vA}{D\ln(1+1/S)}, \tag{1}$$

for a fixed mass flow rate of fuel. Here, v is the mean fuel exit velocity, and A is the fuel nozzle exit area. Since the molecular diffusivity, D, is inversely proportional to pressure, P, i.e. $D \propto 1/P$, then the height of the diffusion flame is independent of the pressure. At a given height above the burner nozzle exit, the average velocity within the flame envelope would not change with pressure, if the flame cross-sectional area varies inversely with pressure. That is, as the pressure increases, the material flow within the flame envelope will

be through a narrower cross-section but at a higher density, thus keeping the average velocity constant at a given height [5,7]. This is the case with methane–air flames at elevated pressures [7]. This implies that the buoyant acceleration estimated by Roper et al. [22] for atmospheric flames is also valid for high-pressure hydrocarbon–air flames to a first approximation. This argument assumes that the air entrainment into the flame envelope does not change much with pressure (this is justified in view of the fact that the product of density and mass diffusion coefficient is invariant of pressure). With methane–oxygen flames, it was observed that the flame diameter is almost inversely proportional to pressure (see Section 3.2, first paragraph). This implies that (a) buoyant acceleration estimated for atmospheric conditions should be applicable to higher pressures, and (b) in flames at various atmospheres, the residence times would be approximately equal at a certain height allowing comparison of soot and temperatures at a given height at different pressures. It should be noted that above argument is valid only for the yellow/orange diffusion flame portion of the methane–oxygen flames.

The molar stoichiometric oxidizer to fuel ratio S is 9.52 for methane–air and it is 2 for methane–oxygen. In Roper's correlations the mean flame temperature is approximated as 1500 K when the oxidant is standard air [22]. Taking the mean flame temperature about 600 K higher in methane–oxygen flames than methane–air flames, for the same mass flow rate methane–oxygen flame height would be about a factor of 5 shorter than that of a methane–air co-flow flame on a circular burner. With a 0.55 mg/s methane flow rate in methane–air flames, the visible height was about 9 mm [7]. Then the height in methane–oxygen flames for the same flow rate of methane, the flame height should be about 1.8 mm, and for a flow rate of 1.1 mg/s methane the height should be doubled per Eq. (1), assuming that the reactant streams in both cases have similar temperatures. These heights correspond to axial positions longer than the heights of the luminous flame regions, Fig. 3, almost mid-point of the blue flame region.

In Roper's formulation, the flame height is taken as the axial location where the equivalence ratio is stoichiometric [21]. In sooting hydrocarbon–air flames, experiments indicate that the flame height to soot oxidation length ratio is constant and close to unity [22]. In methane–oxygen flames the conditions are much different than methane–air flames and Roper's formulation is not expected to apply to methane–oxygen flames at elevated pressures. One of the main reasons is the flame temperatures as stated in the previous paragraph: in methane–oxygen flames measured maximum temperatures were about 500–600 K higher than those in methane–air flames (see Section 3.3 below). The other reason could be the mass diffusivity's variation with pressure. The mass diffusivity's inverse dependence on pressure starts deviating from inverse relationship and the product of pressure and diffusivity is no longer constant but starts decreasing with increasing pressure when the reduced pressure P_r, ratio of actual pressure to the critical pressure of the gas, exceeds about 0.5 [23], up to the critical point. At supercritical pressures, it seems that $D \propto P_r^{1/2}$ [23]. The critical
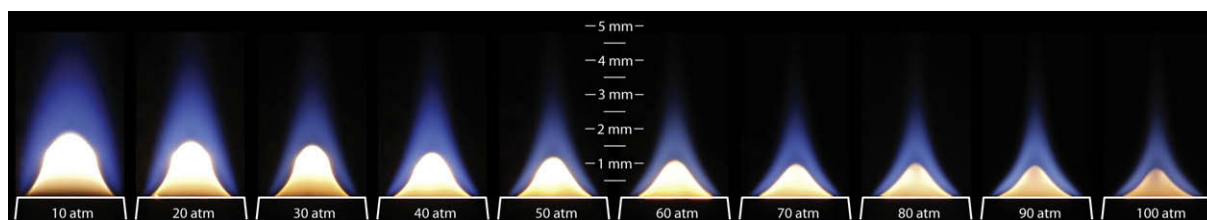

Fig. 6. Images of the methane–oxygen flames from 10 to 100 atm. Methane flow rate is 1.1 mg/s. The luminous flame (the yellow/orange zone) height is about 2 mm at 10 atm and gradually decreases to about 1 mm at 100 atm. (For interpretation of the references to color in this figure legend, the reader is referred to the web version of this article.)

Table 1
Critical properties of methane, oxygen, and nitrogen [24].

Species	Critical pressure, MPa (atm)	Critical temperature, K	Critical density, kg/m^3
Methane, CH_4	4.64 (45.8)	190.8	162.6
Oxygen, O_2	5.09 (50.2)	154.6	436.1
Nitrogen, N_2	3.40 (33.6)	126.3	313.1

pressures and temperatures of methane, oxygen, and nitrogen are listed in Table 1. Above 50 atm, in both methane–air and methane–oxygen flames, conditions are supercritical and the mass diffusivities should be similar in both flames. However, there are strong indications and experimental data that imply that at supercritical pressures absolute concentrations influence the mass diffusivity significantly [23]. It seems that the decrease in height with pressure in methane–oxygen flames could be due to the relatively higher flame temperatures and higher mass diffusivities as well as high concentrations of oxygen leading to higher oxidation rates of soot.

3.2. Soot formation

The variation of the soot volume fraction with pressure, and axial and radial locations are shown in Figs. 7–9. Soot formation was distributed in an annular band near the burner rim. With increasing pressure, the annular soot distribution disappeared and the peak soot concentration occured on the flame centerline similar to the behavior observed in hydrocarbon–air diffusion flames. The contraction of the flame diameter is reflected by the location of the peak soot concentrations as observed in Figs. 7–9. The cross-sectional area of the flame (measured by the radial location of the peak soot concentrations or peak temperatures) showed an almost inverse dependence on pressure between 10 and 40 atm, Fig. 10. At higher pressures, however, the cross-sectional area of the flame decreased sharply and the inverse linear dependence on pressure was lost. When the diameter of the flame was determined based on the diffusive flame boundary of the luminous zone at the flame height of 0.5 mm, the close to unity inverse pressure exponent was restored throughout the entire pressure range as shown in Fig. 10.

A three-dimensional representation of the radial soot volume fraction profiles as a function of pressure is shown in Fig. 11. Peak
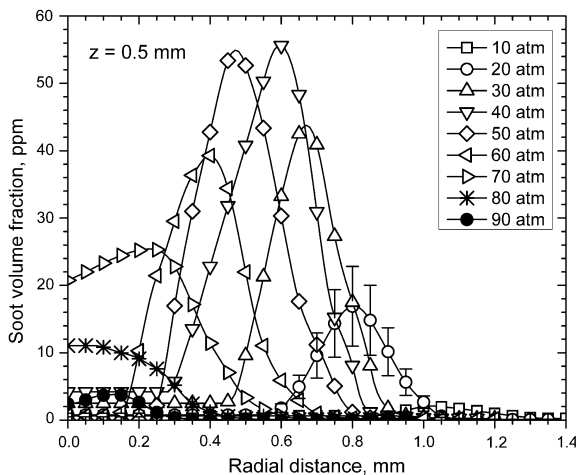

Fig. 8. Soot volume fraction profiles at various pressure at the height of 1 mm in the flame. Methane flow rate is 1.1 mg/s. Error bars correspond to total uncertainties in soot volume fraction with a 95% confidence interval. For clarity error bars are shown for 10 atm data only.
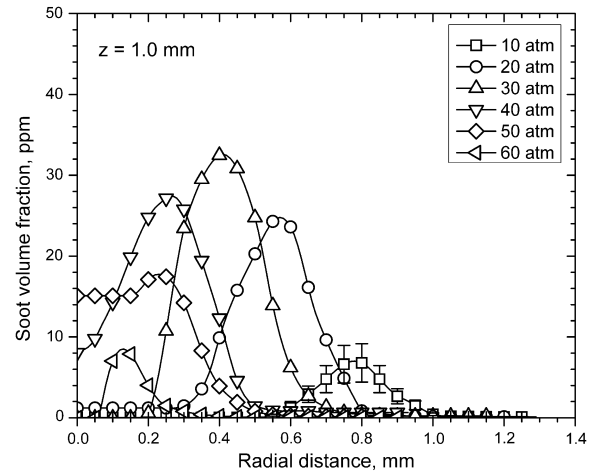
soot volume fraction increased from 7 ppm at 10 atm to over 55 ppm at 40 atm. However, further increase in pressure resulted in a decrease in soot volume fraction to about 4 ppm at 90 atm. Maximum soot volume fraction increases as $f_{v,max} \propto P^{1.5}$ for pressures between 10 and 40 atm. The pressure exponent is -2.3 for pressures between 50 and 70 atm and about -7.6 for 70–90 atm.

As originally suggested in [1] and adopted in our previous studies [5–7], to assess the sensitivity of sooting propensity of the flame to pressure, the percentage of total carbon in the fuel converted to soot as a function of height is a better measure than the maximum line-of-sight integrated soot concentrations. We use the same approach here to understand the influence of pressure. The mass flow rate of carbon, in the form of soot, can be determined, as a function of height, through the relationship

$$\dot{m}_s(z) = v_z(z)\rho_s \int 2\pi r f_v(r,z) dr \qquad (2)$$

where v_z is the axial velocity, $\rho_s = 1.8$ g/cm^3 is the soot density, and z is the axial height. The axial velocity is estimated using the relationship $v_z(z) = \sqrt{2az}$ where a is an acceleration constant commonly as-
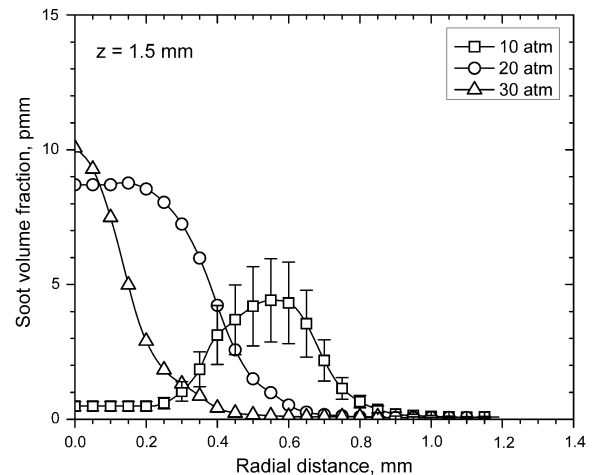

Fig. 7. Soot volume fraction profiles at various pressures at the height of 0.5 mm in the flame. Methane flow rate is 1.1 mg/s. Error bars correspond to total uncertainties in soot volume fraction with a 95% confidence interval. For clarity error bars are shown for 10 atm data only.
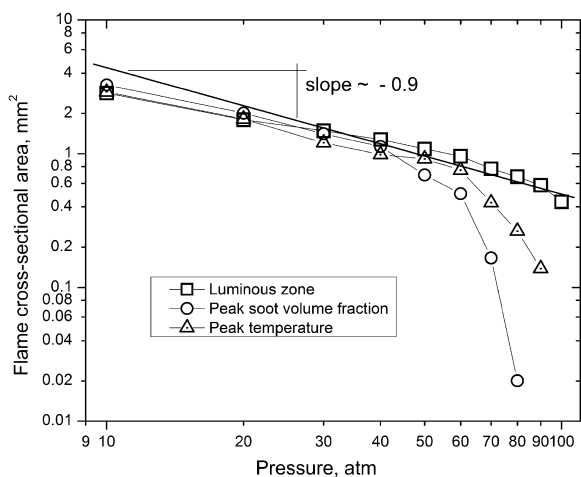

Fig. 9. Soot volume fraction profiles at various pressures at the height of 1.5 mm in the flame. Methane flow rate is 1.1 mg/s. Error bars correspond to total uncertainties in soot volume fraction with a 95% confidence interval. For clarity error bars are shown for 10 atm data only.

Fig. 10. Cross-sectional area of the methane–oxygen flames at pressures from 10 to 100 atm. Luminous zone cross-sectional area was evaluated at flame height of 0.5 mm.
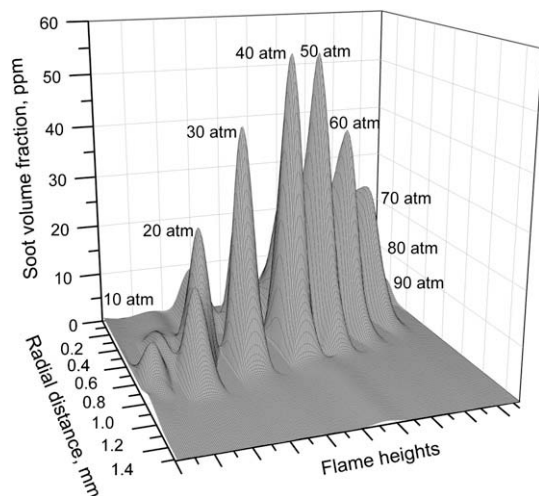

Fig. 11. A three-dimensional rendition of the soot volume fraction as a function of pressure and the spatial location within the flame. It should be noted that the "Flame heights" axis is a repeating coordinate representing successive height locations from the burner tip for each pressure.

Fig. 12. Maximum conversion of fuel's carbon to soot as a function of pressure.

3.3. Flame temperature

Since the spectral soot emission diagnostic technique used in this study measures the soot radiation emission, temperatures can only be determined where there is sufficient soot to provide a resolvable signal. These regions typically occur at radial locations centered about the zones of peak soot volume fraction. Previous characterization of the SSE has shown that temperatures are known to decrease at the outer edges of the annuli earlier than would be predicted by flame models or other experimental diagnostics. Thus the peak temperatures in the reaction zone are under-predicted. It is believed that this fall off is caused by errors introduced through the inversion algorithm when inverting the rapidly decreasing line-of-sight emission intensities at the edge of the flame. Temperatures can also be inaccurate in the core of the flame due to low soot concentrations in the core relative to the peak concentrations in the annulus [5]. Consequently, the radial temperature profiles provided here are limited to annulus regions where sufficient soot exists. It is possible that the limitations of the temperature measurements in the core and on the outside of the soot annulus may be caused by beam steering when the SSE diagnostic is applied on a flame with such intense temperature gradients. In the present study, the uncertainty in the temperature measurements limits the accuracy of the soot volume fraction measurements. Repeated measurements at the same location at different times showed that the temperature data is reproducible within 2% including any anomalies in the temperature values discussed above.

Measured soot temperatures profiles at 10–90 atm are plotted in Figs. 13–15 with 0.5 mm height increments from 0.5 to 1.5 mm. Low down in the flame for the pressures between 10 and 60 atm, there was a general increase in soot temperature with pressure. However, at pressures 70 atm and above, the temperatures decreased with pressure. The same trend was observed at the mid-height of the flame where the temperatures initially increased with pressure then fall when the pressure was increased to 40 atm and above. The highest temperature was measured at the tip of the luminous zone of the flame and it decreased with increasing pressure.

The trend observed by the soot temperature profiles may partially be explained by the fact that the visible flame height diminished with increasing pressure. However, low down in the flame, the temperature continued to decrease at pressures 70 atm and above despite the fact that the flame height remained constant. This suggests that the effect of flame height reduction, if any, is small and there is a stronger overriding effect that is not yet explored. One possible effect could be the influence of Soret diffusion. The direct simulation results of Palle et al. [25] of one-dimensional

sumed to be 25 m/s² [1,5]. The percentage of carbon in the fuel converted to soot is simply $\eta_s = \dot{m}_s / \dot{m}_c$, where $\dot{m}_c$ is the carbon mass flow rate at the nozzle exit. A plot of maximum percentage conversion of carbon to soot as a function of pressure is shown in Fig. 12 as a logarithmic plot. However, a single power–law relationship between the percentage conversion of fuel's carbon to soot and the pressure was not possible at all. Approximate pressure exponents for different pressure intervals are noted on Fig. 12. The pressure sensitivity decreased significantly as pressure reached 40 atm, then the pressure exponent became negative as the pressure was further increased.

The numerical study of high-pressure methane–air flames by Liu et al. [3] show that with increasing pressure air entrainment into the flame near the burner rim increases. A similar behavior is expected to take place with methane–oxygen flames. At near critical and at supercritical pressures, with increased oxygen "leakage" into the base of the flame, the conditions may not be strictly those of a diffusion flame but a partially premixed flame. This could be one of the reasons for decreasing sooting tendency with increasing pressure at supercritical conditions.
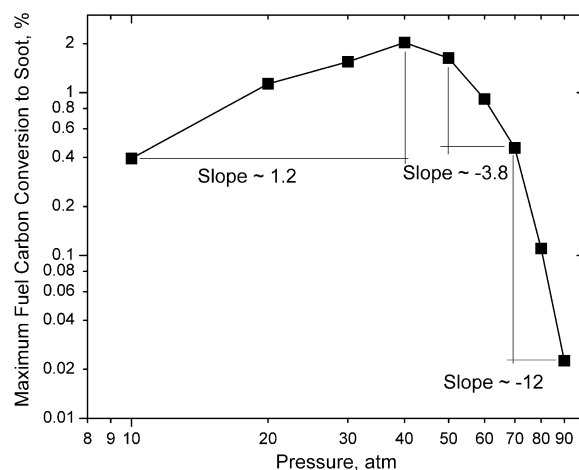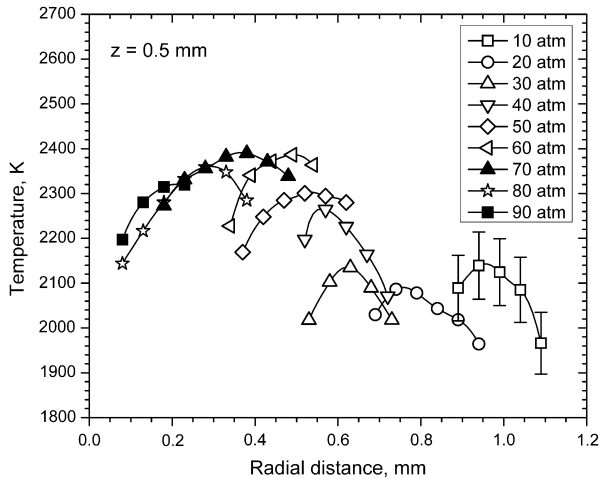
Fig. 13. Radial temperature profiles at various pressures at the flame height of 0.5 mm within the methane–oxygen flames. Error bars correspond to total uncertainties in temperature. For clarity error bars are shown for 10 atm data only.
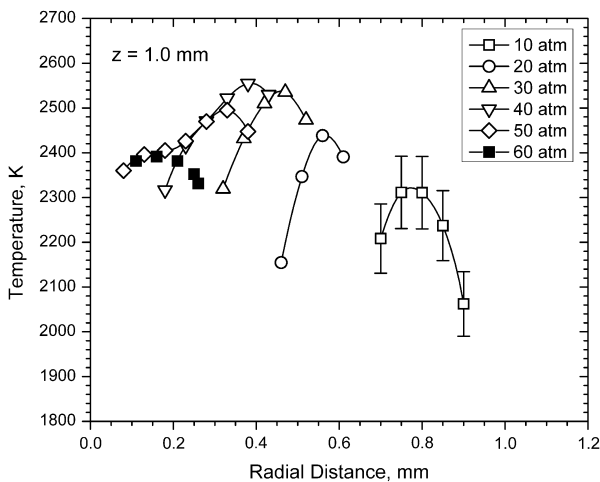

Fig. 14. Radial temperature profiles at various pressures at the flame height of 1 mm within the methane–oxygen flames. Error bars correspond to total uncertainties in temperature. For clarity error bars are shown for 10 atm data only.

Fig. 15. Radial temperature profiles at various pressures at the flame height of 1.5 mm within the methane–oxygen flames. Error bars correspond to total uncertainties in temperature. For clarity error bars are shown for 10 atm data only.
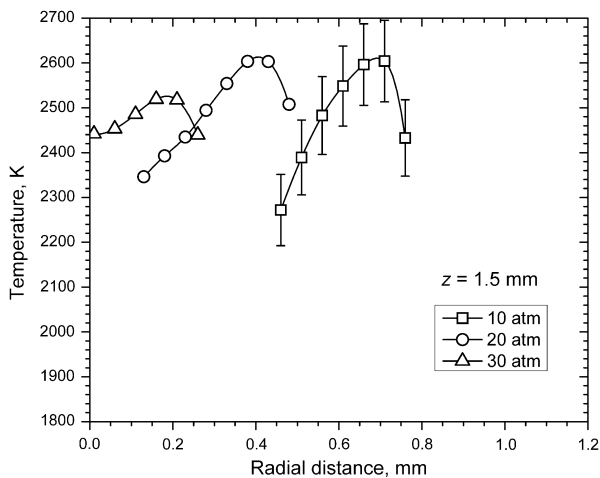
real gas laminar diffusion flames at high pressures show that Soret and Dufour effects are negligible for reactions comprised of species with equal or near equal molecular weights. However, Soret diffusion effects are apparent when species with non-equal molecular weights are involved in the reaction at high pressures and result in reductions of the peak flame temperature. This conclusion was reached upon the results of simulation of a hydrogen–oxygen flame at 100 atm [25] and seems plausible, although the molecular weight discrepancy in methane–oxygen flames is not as large as the difference in hydrogen–oxygen flames. The maximum radial temperature gradients, that could be evaluated from the data in Figs. 13–15, were approximately 2000–4000 K/mm. These gradients are more than twice the gradients observed in high-pressure methane–air flames [7]. Since the driving force in Soret diffusion is the temperature gradient [26], reductions in peak flame temperatures in methane–oxygen flames are more likely than in methane–air flames at high pressures.

3.4. Experimental uncertainty

The soot particles in the flame absorb and emit radiation, thus emissions from soot are inherently attenuated by other soot particles along the detection path in the flame. However, the cross-sectional area of the flame decreased with pressure so the length at which the emissions are attenuated is shortened. Since the attenuation of emission is a function of the product of the soot concentration and the absorption path length, attenuation by soot particles in the flame is assumed negligible. Furthermore, the flame emission model presented in [16] showed that attenuation of emission by soot particles introduced only a small error into the measurements (i.e. <2%). Thus, no attenuation correction was applied to the data even for the highest soot loadings observed in the study. It is difficult to quantify the errors introduced by potential changes in the morphology and optical properties of soot with pressure, and by using pure oxygen as the oxidizer instead of air. There is a lack of experimental data on soot aggregate size (that is the number of primary soot particles per aggregate) and soot morphology (that could be expressed in terms of fractal characteristics of the aggregates). Limited data on primary particle size, for example, obtained in a diesel engine [27] and in a shock tube [28] are not in agreement on whether the pressure has any effect on mean soot size. The total uncertainties in the temperature and soot volume fraction measurements were estimated as 3.5% and 40%, respectively, with a 95% confidence interval. Error bars in Figs. 7–9 and 13–15 correspond to these uncertainties.

It should be noted that above uncertainties include contributions from the Abel inversion process as well. Details of extensive error analysis, including uncertainties originating from the uncertainty in soot refractive index, are given in [5,29].

Heat losses to the burner fuel tube and the sintered metal foam is significant because of very short flames. The heated foam would be transferring some of this heat to the fuel stream contributing to fuel's thermal decomposition/pyrolysis and possibly accelerating soot formation. Assuming that the heat losses do not change significantly with changing pressure, the effect would be similar at all pressures. However, this assumption may not be justified and detailed modelling of the flame at high pressures, including the heating of the fuel stream by heated foam and fuel tube, could provide the answer. The effect of heat loss to the fuel tube at atmospheric conditions is discussed in [30].

4. Concluding remarks

The present work examined the methane–oxygen co-flow diffusion flame structure at elevated pressures up to 100 atm. Spectral

soot emission was used to measure the soot volume fraction and soot temperature within the flame at pressures up to 90 atm. Two constant methane mass flow rates of 0.55 and 1.1 mg/s were used, although detailed high-pressure measurements were provided for the higher flow rate only. At the higher 1.1 mg/s methane flow rate, the height of the luminous zone, marked by the visible soot radiation emission, decreased most notably between 10 and 50 atm. At pressures 60 atm and higher, the height remained relatively constant at about 1 mm. Overall, increasing the pressure from 10 to 100 atm resulted in over 50% reduction in the height of the luminous zone. Methane–oxygen flames were much hotter than the methane–air flames as expected. At pressures between 10 and 40 atm, the cross-sectional area of the flame (measured by the radial location of maximum soot concentration) showed a linear inverse dependence on pressure. At pressures beyond 40 atm, the flame cross-sectional area decreased sharply, despite the fact that the physical flame boundary of the luminous zone remained relatively unaltered. Maximum soot volume fraction of 55 ppm was recorded at 40 atm. However, at 90 atm, soot volume fraction decreased to about 4 ppm. Soot temperature measurements showed that temperatures increased with pressure in the lower range of pressures. In the higher pressure range, however, temperature showed an inverse dependence on pressure.

Acknowledgments

References

[1] W.L. Flower, C.T. Bowman, Proc. Combust. Inst. 21 (1988) 1115–1124.
[2] W. Lee, Y.D. Na, JSME Int. J. Ser. B 43 (4) (2000) 550–555.
[3] F. Liu, K.A. Thomson, H. Guo, G.J. Smallwood, Combust. Flame 146 (2006) 456–471.
[4] L.L. McCrain, W.L. Roberts, Combust. Flame 140 (2005) 60–69.
[5] K.A. Thomson, Ö.L. Gülder, E.J. Weckman, R.A. Fraser, G.J. Smallwood, D.R. Snelling, Combust. Flame 140 (2005) 222–232.
[6] D.S. Bento, K.A. Thomson, Ö.L. Gülder, Combust. Flame 145 (2006) 765–778.
[7] H.I. Joo, Ö.L. Gülder, Proc. Combust. Inst. 22 (2009) 769–775.
[8] J. Lux, O. Haidn, J. Prop, Power 25 (1) (2009) 15–23.
[9] G. Sugiyama, Proc. Comb. Inst. 25 (1994) 601–608.
[10] K.-O. Lee, C.M. Megaridis, S. Zelepouga, A.V. Savaliev, L.A. Kennedy, O. Charon, S. Ammouri, Combust. Flame 121 (2000) 323–333.
[11] D.X. Du, R.L. Axelbaum, C.K. Law, Proc. Combust. Inst. 23 (1990) 1501–1507.
[12] L. Pons, N. Darabiha, S. Candel, G. Ribert, V. Yang, Combust. Theor. Model. 13 (2009) 57–81.
[13] N. Zong, V. Yang, Proc. Combust. Inst. 31 (2007) 2309–2317.
[14] B.A. Palyonov, A.I. Bessonov, A.I. Pastuhov, S.S. Shulkova, G.P. Kalmykov, in: C. Bruno, A.G. Accettura (Eds.), Advanced Propulsion Systems and Technologies, Today to 2020, vol. 23, AIAA Progress in Aeronautics and Astronautics, 2008, pp. 163–171.
[15] C.J. Dasch, Appl. Opt. 31 (8) (1992) 1146–1152.
[16] D.R. Snelling, K.A. Thomson, G.J. Smallwood, Ö.L. Gülder, E.J. Weckman, R.A. Fraser, AIAA J. 40 (9) (2002) 1789–1795.
[17] G. Singla, P. Scouflaire, C. Rolon, S. Candel, Proc. Combust. Inst. 30 (2005) 2921–2928.
[18] K. Saito, F.A. Williams, A.S. Gordon, Combust. Sci. Technol. 47 (1986) 117–138.
[19] S.A. Northrup, C.P. Groth, Solution of Laminar Diffusion Flames using a Parallel Adaptive Mesh Refinement Algorithm, AIAA Paper No: AIAA2005-547, 2005.
[20] M.R.J. Charest, C.P.T. Groth, Ö.L. Gülder, Numerical Prediction of Sooting Laminar Diffusion Flames Using Adaptive Mesh Refinement, in: 6th US National Combustion Meeting, May 18–20, Ann Arbor, MI, 2009.
[21] F.G. Roper, Combust. Flame 29 (1977) 219–226.
[22] F.G. Roper, C. Smith, A.C. Cunningham, Combust. Flame 29 (1977) 227–234.
[23] R.C. Reid, J.M. Prausnitz, B.E. Poling, The Properties of Gases and Liquids, 4th ed., McGraw Hill, 1987 (Chapter 11).
[24] N.B. Vargaftik, Y.K. Vinogradov, V.S. Yargin, Handbook of Physical Properties of Liquids and Gases, 3rd ed., Begell House, 1996.
[25] S. Palle, C. Nolan, R.S. Miller, Phys. Fluids 17 (2005) 103601-19.
[26] K. Harstad, Ind. Eng. Chem. Res. 48 (2009) 6907–6915.
[27] R. Ryser, T. Gerber, T. Dreier, Combust. Flame 156 (2009) 120–129.
[28] H. Kellerer, R. Koch, S. Wittig, Combust. Flame 120 (2000) 188–199.
[29] K.A. Thomson, PhD Thesis, University of Waterloo, Waterloo, Canada, 2004.
[30] Ö.L. Gülder, K.A. Thomson, D.R. Snelling, Combust. Flame 144 (2006) 426–433.